Inorganic Chemistry

pubs.acs.org/IC Article

Origin of Unprecedented Formation and Reactivity of Fe^{IV}=O Species via Oxygen Activation: Role of Noncovalent Interactions and Magnetic Coupling

Asmita Sen, Neethinathan Johnee Britto, Dustin Kass, Kallol Ray,* and Gopalan Rajaraman*

Cite This: *Inorg. Chem.* 2024, 63, 9809−9822 Read Online

ACCESS | Metrics & More | Article Recommendations | Supporting Information

ABSTRACT: Emulating the capabilities of the soluble methane monooxygenase (sMMO) enzymes, which effortlessly activate oxygen at diiron(II) centers to form a reactive diiron(IV) intermediate Q, which then performs the challenging oxidation of methane to methanol, poses a significant challenge. Very recently, one of us reported the mononuclear complex $[(cyclam)Fe^{II}(CH_3CN)_2]^{2+}$ (**1**), which performed a rare bimolecular activation of the molecule of O_2 to generate two molecules of Fe^{IV}=O without the requirement of external proton or electron sources, similar to sMMO. In the present study, we employed the density functional theory (DFT) calculations to investigate this unique mechanism of O_2 activation. We show that secondary hydrogen-bonding interactions between ligand N−H groups and O_2 play a vital role in reducing the energy barrier associated with the initial O_2 binding at **1** and O−O bond cleavage to form the Fe^{IV}=O complex. Further, the unique reactivity of Fe^{IV}=O species toward simultaneous C−H and O−H bond activation process has been demonstrated. Our study unveils that the nature of the magnetic coupling between the diiron centers is also crucial. Given that the influence of magnetic coupling and noncovalent interactions in catalysis remains largely unexplored, this unexplored realm presents numerous avenues for experimental chemists to develop novel structural and functional analogues of sMMO.

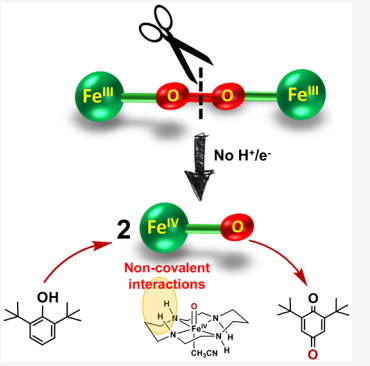

INTRODUCTION

High-valent Fe^{IV}=O species are popular reactive intermediates in oxidative transformations catalyzed by monomeric and dimeric metalloenzymes.[1−6] However, the mechanism of the formation of these key intermediates in dinuclear enzymes is very different from that of mononuclear ones. At monomeric iron metalloenzymes, molecular dioxygen (O_2) is activated by the formation of $\{FeO_2\}$ adducts such as Fe^{III}−superoxo ($Fe^{III}-O_2^{-\bullet}$) and Fe^{III}−(hydro)peroxo intermediates,[3] which undergo O−O bond cleavage resulting in the formation of the catalytically active Fe^{IV}=O species.[4,5] In contrast, in the dinuclear enzymes, direct activation of dioxygen takes place without the involvement of any additional proton or electron sources, resulting in either an open $(L)Fe^{IV}-O-Fe^{IV}(L)$ or closed bis(μ-oxo)diiron(IV) species.[7−9] The formation of the majority of biomimic Fe^{IV}=O species relies on the presence of both electron and proton donors, imitating the mononuclear iron metalloenzymes. However, bimolecular activation of dioxygen at iron(II) centers similar to that observed in the highly coveted soluble methane monooxygenase (sMMO) enzymes,[10−12] has stayed elusive in model complexes until very recently.

Ray and co-workers reported a novel direct dioxygen activation in a cyclam-based Fe^{II} model system forming Fe^{IV}=O species without any proton or electron donors (see Scheme 1).[13] Experimentally, the $[(cyclam)Fe(CH_3CN)_2]^{2+}$ (**1**) species reacts with molecular dioxygen in acetone at −20 °C, resulting in the formation of a room-temperature-stable terminal Fe^{IV}=O species, $[(cyclam)Fe(CH_3CN)(O)]^{2+}$(**2**), following second-order kinetics. Although clear evidence for the formation of an $Fe^{III}-O_2^{-\bullet}$ intermediate on the way to the generation of the putative Fe^{IV}=O species is observed (Scheme 2), the thermodynamic factors leading to the conversion of **1** to **2** are not well-understood. Furthermore, complex **2** was shown to react with 1 equiv. of 2,6-di-*tert*-butylphenol (DTBP), resulting in 32% formation of 2,6-di-*tert*-butyl-1,4-benzoquinone (DTQ, **p**) as a major product. Intriguingly, this conversion requires both O−H bond activation and regioselective C−H bond activation, which are unprecedented for Fe^{IV}=O species. Given that complex **2** shows unique reactivity and is formed by a mechanism reminiscent of those generated by sMMO enzymes, unraveling the underlying energetics of the reaction becomes pivotal for designing a robust catalyst capable of mimicking or even

Received: January 27, 2024
Revised: March 25, 2024
Accepted: April 22, 2024
Published: May 13, 2024

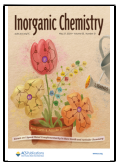

https://doi.org/10.1021/acs.inorgchem.4c00371
Inorg. Chem. 2024, 63, 9809−9822

Scheme 1. Comparison of Overall Reaction of O_2 with Chosen Model Complex 1 and sMMO Enzyme

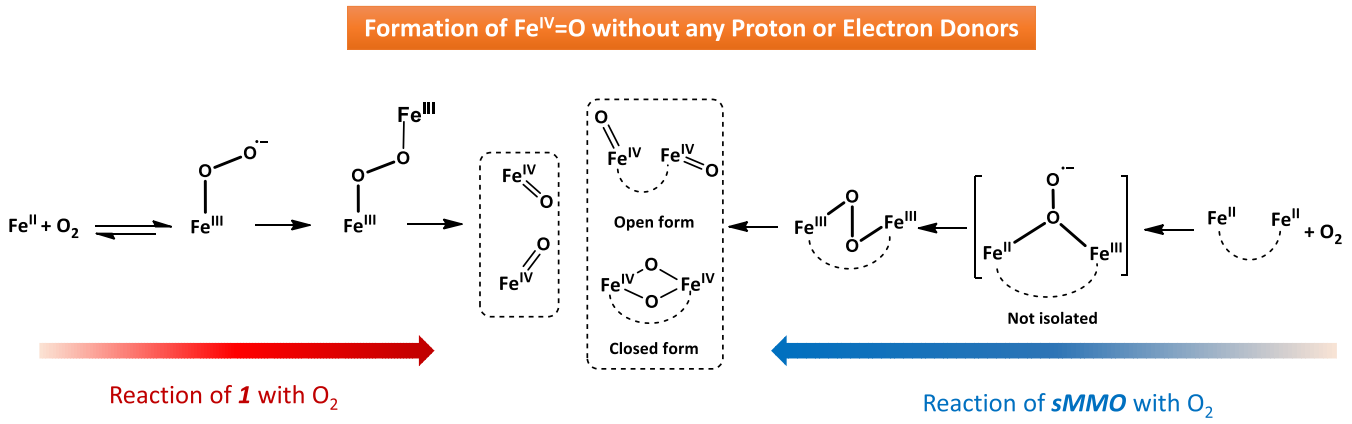

Scheme 2. Formation of $[(cyclam)Fe(CH_3CN)(O)]^{2+}$(2) from $[(cyclam)Fe(CH_3CN)_2]^{2+}$ (1) via $Fe^{III}-O_2^{-\bullet}$ Species (int1) and Further C−H/O−H Bond Activation Reaction

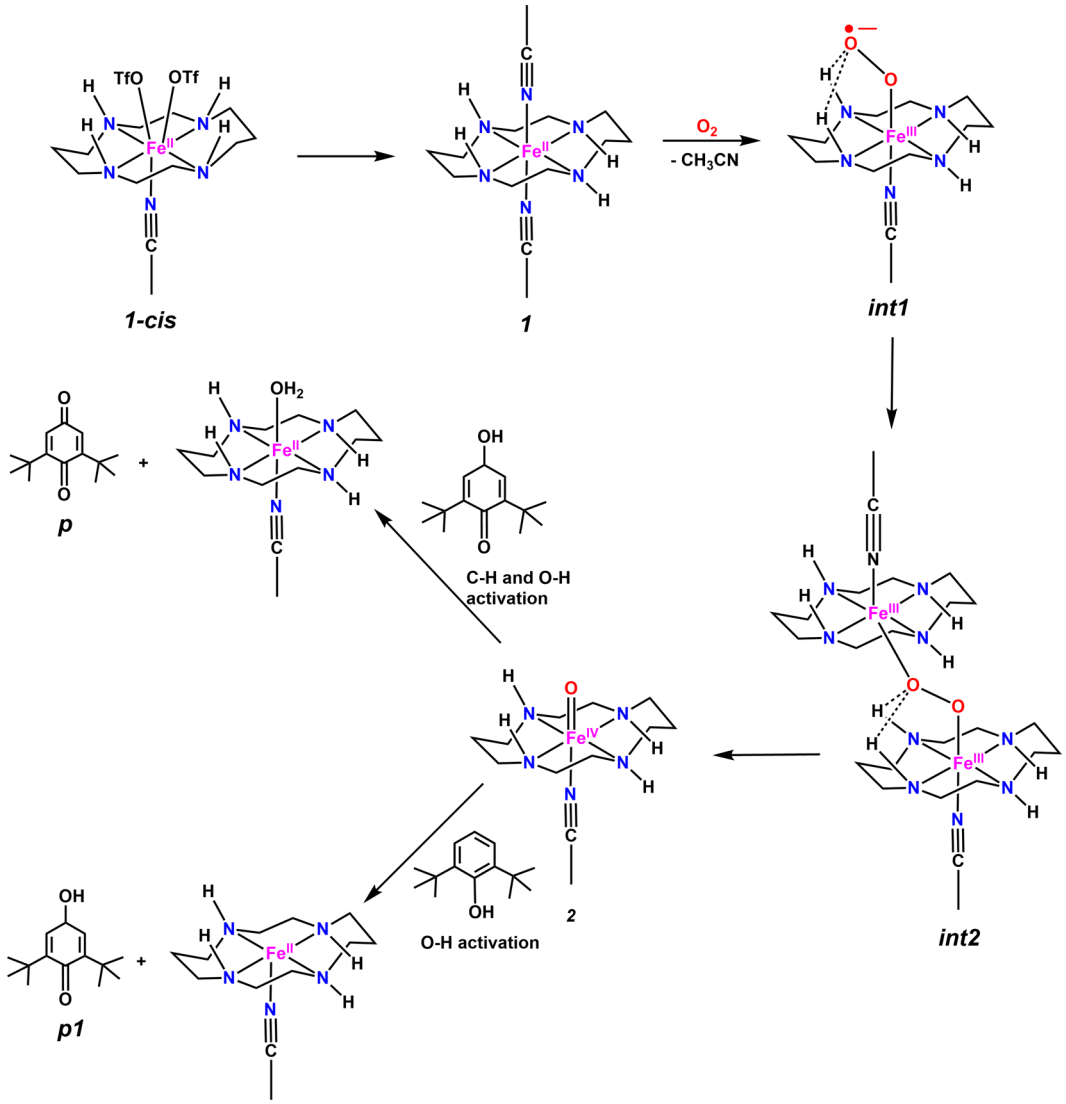

outperforming the catalytic activity exhibited by sMMO enzymes.[14]

Accordingly, in this work, by employing density functional theory (DFT) calculations, we aim to answer the following intriguing questions: (i) What is the step-by-step mechanism leading to the conversion of **1** to **2**, and what makes this transformation distinctively unique? (ii) What is the origin of the unique reactivity of **2** with phenols leading to the unprecedented activation of both C−H and O−H bonds?

https://doi.org/10.1021/acs.inorgchem.4c00371
Inorg. Chem. 2024, 63, 9809−9822

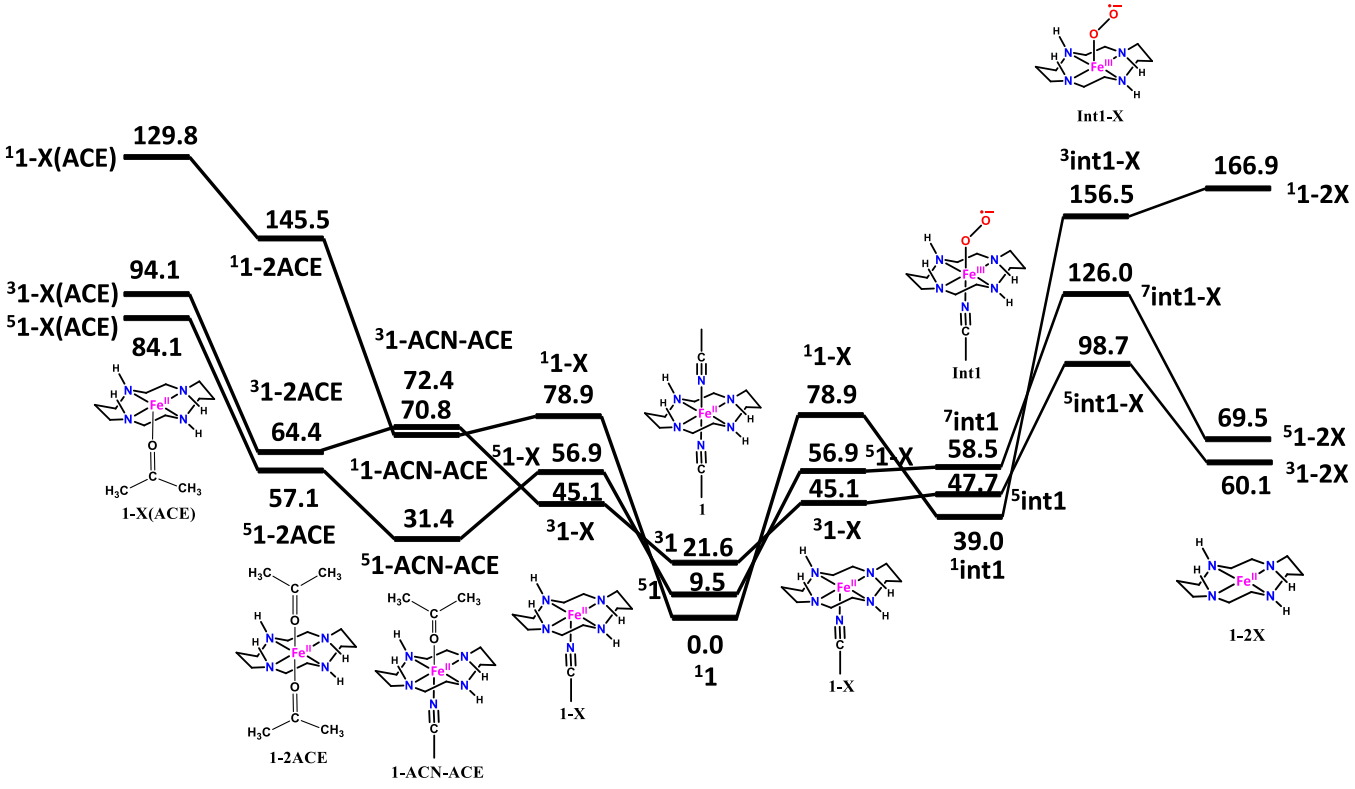

Figure 1. DFT-computed potential energy surface diagram for stepwise formation of ^{1}**int1**. All energies are given in kJ/mol.

(iii) What are the diverse factors that govern the overall reactivity of **2**?

COMPUTATIONAL DETAILS

Geometries of all stationary points were optimized without any restrictions by DFT calculations using Gaussian 16 (Revision C.01) suite of program.[15] The hybrid unrestricted B3LYP density functional[16,17] was employed in conjunction with the triple-ζ-quality LANL2TZ basis set[18] with the Los Alamos effective core potential for the metal (Fe) and the 6-31G** basis set for H, C, O, and N centers. Employing a slightly higher basis set (LANL2TZ for Fe and 6-311G** for H, C, O, and N) yields similar spin-state ordering, with the gap found to vary marginally for **1** (within 4 kJ/mol). The functional was chosen based on the earlier literature and benchmarking available on similar systems and the ability of B3LYP functional to interpret a correct ground state for the Fe^{IV}═O species.[19,20] A comprehensive benchmark investigation conducted by de Visser and colleagues, focusing on the non-heme Fe^{IV}═O-catalyzed sulfoxidation of thioanisole utilizing diverse DFT functionals (B3LYP, BP86, and PBE0) and basis sets revealed the superior ability of the B3LYP functional to accurately replicate both the experimental trends and absolute values of the free energy of activation.[21] Our group has also investigated a series of oxidative transformations employing various heme/non-heme ferryl−oxo complexes and explored a spectrum of density functionals, including B3LYP, B97-D, ωB97X-D, and M06-2X.[22−25] Our analysis revealed that the B3LYP and ωB97X-D functionals consistently produce accurate ground states for all of the species examined. Lundberg and Siegbahn conducted a separate study by employing multiple functionals (BLYP, B3LYP, B3LYP*, and B98) to calculate the O−H bond lengths and energies in hexa-aqua and -hydroxyl Mn complexes.[26] Their research lends further support to the viability of the B3LYP functional in accurately reproducing the correct structural characteristics. Hence, for the current investigation, we opted for the B3LYP formalism, which is renowned for its accurate reproduction of structural parameters, spin-state energetics, and spectroscopic properties. Moreover, concerning dinuclear Fe complexes, numerous benchmarks substantiate the superiority of B3LYP over other functionals.[27−32] Furthermore, Grimme's D3 dispersion correction was also included in the calculation.[33]

Harmonic vibrational frequency calculations were conducted to characterize the properties of all stationary points and to determine the zero-point energy (ZPE) corrections associated with them. All global minima are defined by all positive frequencies, whereas the transition state is distinguished by a single imaginary frequency. Intrinsic reaction coordinate (IRC) calculations were executed at the same computational level to validate the connection of transition states to the minima on both sides of the first-order saddle point. Energy refinement was accomplished through single-point calculations on the optimized geometries, employing the same level of theory with an all-electron def2-TZVP basis set.[34,35] The solvent effect was incorporated into the final higher-level energies using the SMD solvation model in acetone as the solvent.[36] The final energies considered in this study are the ZPE-corrected solvation energies at the higher level. The exchange interaction values (J) were calculated from the energy differences between the high-spin (HS) and low-spin (BS) states determined by the broken symmetry (BS) approach developed by Noodleman[37,38] using the formula

$$J = -\frac{\mathrm{HS} - \mathrm{BS}}{2S_1S_2 - S_2}$$

https://doi.org/10.1021/acs.inorgchem.4c00371
Inorg. Chem. 2024, 63, 9809−9822

Scheme 3. Schematic Representation of the Formation of (1) Followed by the Hydrogen Atom Abstraction Pprocess Forming 2,6-Di-*tert*-butyl-1,4-benzoquinone (DTQ, p), and 2,2′,6,6′-Tetra-*tert*-butyl-1,1′-biphenol (DTP, p′) from 2,6-Di-*tert*-butylphenol (DTBP) [The TMC Ligand Is Shown in the Inset]

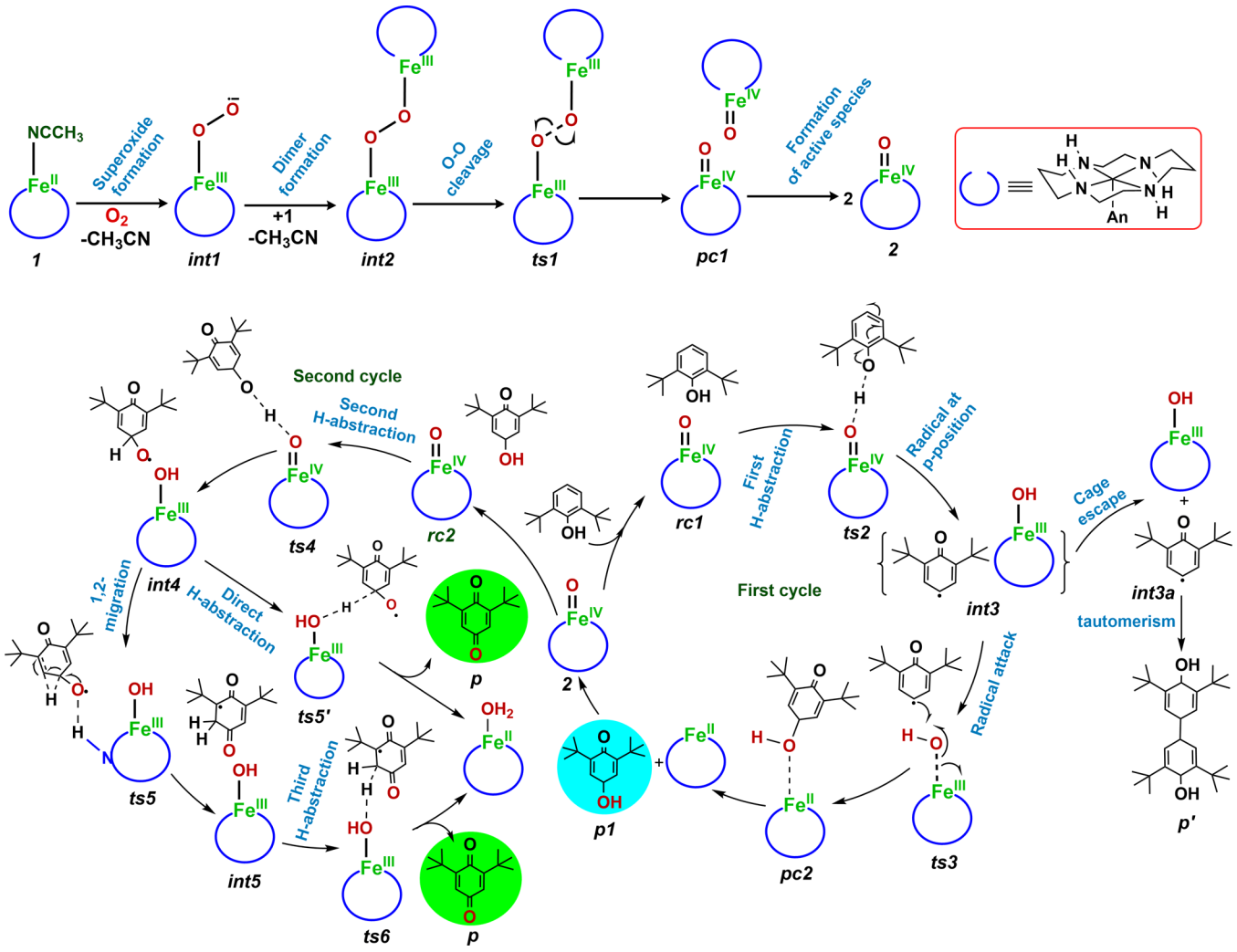

Here, S_1 and S_2 are the spin-states of the individual centers and S_2 is the lower one if they are different. Negative and positive values for J correspond to antiferromagnetic and ferromagnetic interactions, respectively.

All spectroscopic parameters were calculated using the ORCA 5.0 program.[39] The time-dependent DFT (TD-DFT) calculations were performed by employing the UKS/B3LYP methodology with the TZVP basis set.[40,41] The CPCM solvation model was used with acetone as the solvent, as has been recommended for spectral feature calculations.[42] For the zero-field splitting calculations, a state-averaged CASSCF/NEVPT2 method was employed. The starting guess orbitals were obtained by the DFT method employing the ROKS/BP86 terminology with the ZORA-def2-TZVP basis set for Fe, ZORA-def2-TZVP(-f) basis set for N, and O, and ZORA-def2-SVP basis set for the rest of the atoms (C and H). An active space of CAS(n,5) was used, including four electrons in the five 3d orbitals of the metal. For d^4 systems, 5 quintet, 45 triplet, and 50 singlet roots were used. Mössbauer isomer shifts were calculated using UKS/BP86 methodology with the def2-TZVP basis set, based on the calibration constants reported by Römelt et al.[43] All stationary points are denoted as $^{2S+1}\mathbf{Y}_c$, where, "**Y**" is "**rc**" for reactant complex, "**int**" for intermediates, and "**ts**" for transition states and the subscript "c" denotes the nature of the spins if two different paramagnetic centers are present. For instance, the subscript "(hs,hs)" denotes the spin states of the two paramagnetic centers, while "u" or "d" in "(hs,u)" or "(hs,d)" represents the up spin or down spin of the radical on the substrate. Here "hs", "is", and "ls" denote high spin, intermediate spin, and low spin, respectively. The overall spin multiplicity ($2S + 1$) is stated as a left superscript. The AIM2000 program[44] was used to perform topological analysis on selected species using wave functions generated at the same level of theory used for optimization. The isosurface values for the spin-density plots is given as 0.03.

RESULTS

Mechanism of the Formation of Fe^{IV}=O Species. Our calculations reveal that **1** has a low-spin diamagnetic $S = 0$ ground state, with other $S = 2$ and $S = 1$ spin states lying 9.5 kJ/mol and 21.6 kJ/mol higher in energy, respectively (Figure 1). This is consistent with the experimental Mössbauer and NMR spectroscopic data.[13] Two conformers, *cis* (**1-*cis***) and *trans* (**1**), are reported for **1**, with the *trans* conformer (**1**) being more stable, and the observed dioxygen reactivity was attributed to this isomer; therefore, we have restricted our

https://doi.org/10.1021/acs.inorgchem.4c00371
Inorg. Chem. 2024, 63, 9809−9822

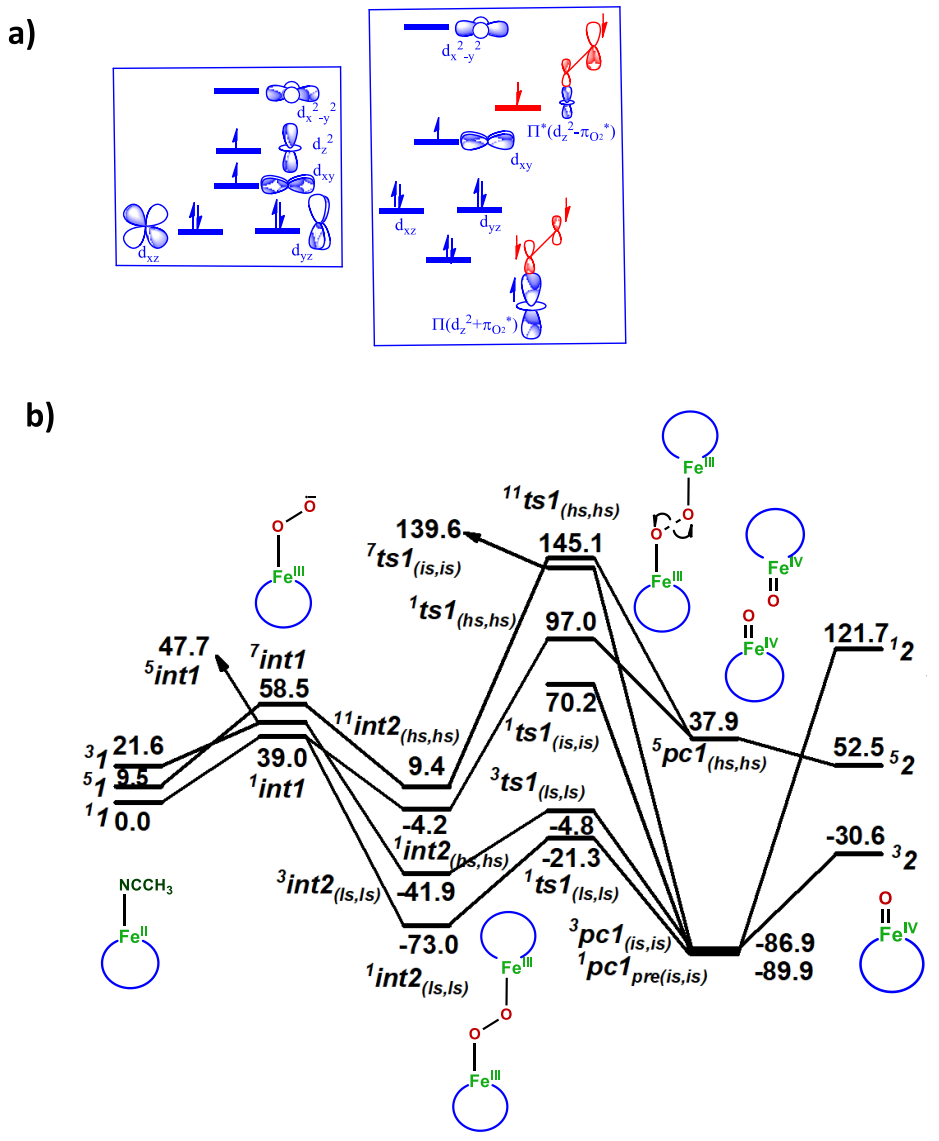

Figure 2. (a) Orbital evolution diagram showing the formation of the singlet superoxo species from the triplet 1-X spin state, (b) DFT-computed potential energy surface diagram for the formation of Fe^{IV}=O species, $[(cyclam)Fe(CH_3CN)(O)]^{2+}$ (**2**) from an Fe^{II} species, $[(cyclam)Fe(CH_3CN)_2]^{2+}$ (**1**).

study to this conformer only. Furthermore, the higher stability of **1** compared to **1-*cis*** is consistent with the experimental findings that the *cis* isomer converts to the *trans* isomer in solution upon stirring over a period of 24 h.[13,45] The mechanism adapted for the oxygen activation by **1** is shown in Scheme 3. Figure 1 depicts the potential energy surface for the stepwise formation of **int1** from **1** via a dissociative mechanism. The reaction begins with the formation of an Fe^{III}–superoxide (Fe^{III}–$O_2^{-\bullet}$) species, $[(cyclam)Fe(CH_3CN)(O_2^{-\bullet})]^{2+}$ (**int1**). This species has an $S = 0$ ground state arising from strong antiferromagnetic coupling ($J = -24.1$ cm^{-1}) between the low-spin $S = {}^1/_2$ Fe^{III} center and the superoxide radical ($O_2^{-\bullet}$) species, which is also supported by experimental data. The formation of **int1** is endothermic by 39 kJ/mol in CH_3CN, whereby both the CH_3CN ligands are bound to the Fe(II) center, giving an $S = 0$ ground state for **1**. This explains why no dioxygen activation occurs in CH_3CN. In contrast, in acetone solutions of **1**, the dissociation of one axial acetonitrile leads to the formation of a five-coordinate species (represented as **1-X** in Figure 1), which is now stabilized in an $S = 1$ state. The conversion of **1** to **1-X** is calculated to be endoergic by 45.1 kJ/mol at the triplet state, while the quintet and singlet species are, respectively, 11.8 and 33.8 kJ/mol higher in energy. Notably, the zero-field Mössbauer spectrum of **1** in acetone (Figure S1a) reveals three quadrupole doublets corresponding to low-spin Fe(II) ($\delta = 0.54$ mm s^{-1}, $\Delta E_Q =$ 0.61 mm s^{-1}; 64%), intermediate spin Fe(II) ($\delta = 0.82$ mm s^{-1}, $\Delta E_Q = 1.30$ mm s^{-1}; 22%), and high-spin Fe(II) ($\delta = 0.75$ mm s^{-1}, $\Delta E_Q = 3.52$ mm s^{-1}; 14%) centers. In contrast, a single quadrupole doublet with $\delta = 0.54$ mm s^{-1} and $\Delta E_Q =$ 0.61 mm s^{-1} is obtained in CH_3CN (Figure S1). Thus, in contrast to CH_3CN, where ^{1}**1** is the only species present in solution, in acetone ^{1}**1** exists in equilibrium with ^{3}**1-X** and ^{5}**1-X**, which are formed upon replacement of one CH_3CN ligand in **1**. This equilibrium is expected, with the computed energy difference between ^{3}**1-X** and ^{5}**1-X** being only around 10 kJ/mol. In order to check whether the experimentally assigned ΔE_Q and isomer shifts belong to the five-coordinate intermediate (**1-X**), both of these parameters were computationally calculated for triplet-ground-state species of **1-X**. The

https://doi.org/10.1021/acs.inorgchem.4c00371
Inorg. Chem. 2024, 63, 9809−9822

computed results (δ = 0.87 mm s^{-1}, ΔE_Q = 1.45 mm s^{-1}) were in good concurrence with the experimental values (δ = 0.82 mm s^{-1}, ΔE_Q = 1.30 mm s^{-1}), suggesting that the experimental ΔE_Q and isomer shifts belong to the five-coordinate intermediate proposed. The formation of ^{1}**int1** by dioxygen activation at the paramagnetic ^{3}**1-X** and ^{5}**1-X** states is now exothermic by 6.1 and 17.9 kJ/mol, respectively. The orbital evolution diagram depicted in Figure 2a demonstrates the interaction of ^{3}**1-X** with the approaching triplet dioxygen in an antiferromagnetic manner to yield a singlet Fe^{III}−superoxide (^{1}**int1**).[46−51] The possibility of further dissociation of the second axial acetonitrile ligand, leading to the formation of **1-2X**, and also the possibility of dissociation of another acetonitrile after the dioxygen addition, denoted as **int1-X**, were evaluated. However, both species were found to be relatively more endoergic (Figure 1), allowing us to preclude the possibility of the formation of these species in solution. Experimentally, the reaction was found to be facilitated in acetone solvent, and therefore, we calculated the formation energies for coordination of one acetone molecule (**1-ACN-ACE**), coordination of two acetone molecules (**1-2ACE**), or a five-coordinate species with acetone in the axial position (**1-X(ACE)**). Figure 1 illustrates that the coordination of acetone to **1-X**, yielding **1-ACN-ACE**, is expected to proceed through a spin crossover to the quintet ground state from the triplet, and the reaction is slightly exothermic by −13.7 kJ/mol relative to that of ^{5}**1-X**. The formation of other acetone-bound species, such as ^{5}**1-2ACE** and ^{5}**1-X(ACE)**, was found to be significantly uphill. In particular, the formation of ^{5}**1-X(ACE)**, crucial for O_2 coordination, is highly endothermic by 84.1 kJ/mol. This clearly indicates that the possibility of acetone coordination in the axial position is unlikely and that acetone only plays the role of solvent in the secondary coordination sphere. This also suggests that the mechanism likely proceeds via the formation of the ^{3}**1-X** intermediate. The computed spin density values of ^{1}**int1** suggest strong spin polarization with a drastic variation in the spin density of proximal and distal oxygens (1.136, −0.350, and −0.664 for Fe, O1, and O2, respectively; Table S1). From the optimized geometry of ^{1}**int1** shown in Figure 3a, it is interesting to note the presence of two hydrogen-bonding interactions between the distal oxygen atom (O2) and the two N−H groups above the plane of the cyclam ligand, with a bond distance of 2.425 Å. In order to confirm these noncovalent interactions, quantum theory of atoms in molecules (QTAIM) analysis was performed. The existence of (3, −1) bond critical points (BCPs) in a bond path confirms the presence of the hydrogen-bonding interactions. The molecular graph obtained from QTAIM analysis (Figure 3a) shows the existence of BCPs between the O2 and N−H groups of the cyclam ligand (circled in green), confirming the presence of these two hydrogen-bonding interactions in ^{1}**int1**. Further analysis of the BCPs of the two hydrogen bonds indicates that electron density (ρ) at these points is around 0.0172 au. From the ρ values, the calculated stabilization energy offered by each of the hydrogen-bonding interactions in ^{1}**int1** is around 20 kJ/mol, revealing a rather strong interaction. These hydrogen-bonding interactions play a key role in facilitating strong anchoring of the incoming oxygen and stabilizing the formation energy of ^{1}**int1** by around 15 kJ/mol relative to **1-X**. To verify the theoretical proposal that N−H protons interact with the oxygen atom of the Fe^{III}−superoxo species, the kinetic isotope effect resulting from substituting N−H by N−D was measured. This experiment yielded a kinetic isotope effect of 1.34 (Figure S1b) for the rate

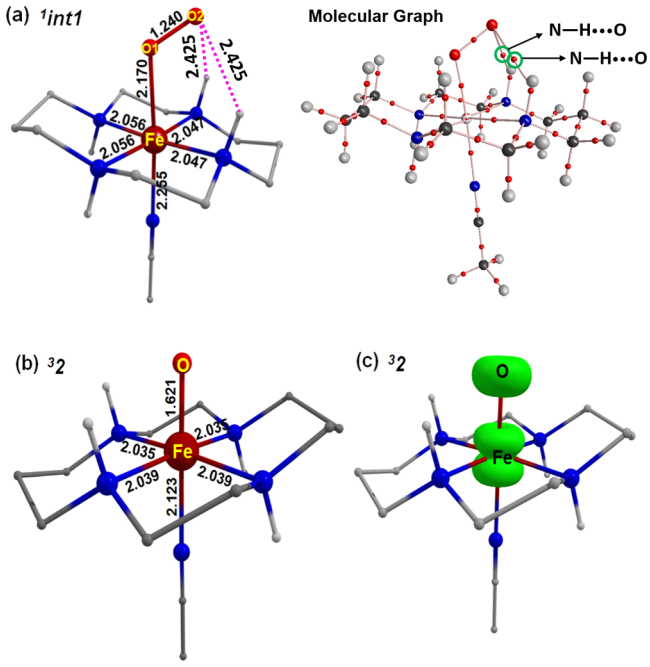

Figure 3. DFT computed optimized structure of (a) ^{1}**int1** (left) and corresponding molecular graph generated from QTAIM analysis (right), (b) Optimized geometry and (c) spin density of ^{3}2. The Fe, O, N, C and hydrogens are shown in brown, red, blue, gray, and white color, respectively.

of formation of ^{1}**int1** when the four −NH groups of the cyclam ligand are substituted by −ND, corroborating the involvement of hydrogen-bonding interactions in the stabilization of ^{1}**int1**.

In the following step, **int1** reacts with another molecule of species ^{3,5}**1-X**, resulting in the formation of a dinuclear Fe^{III}−O−O−Fe^{III} species (**int2**). This is consistent with the experimental observation where a pre-equilibrium release of O_2 from **int1** generates a minor quantity of **1**.[13] In the next step, **int2** undergoes homolytic O−O bond cleavage via **ts1**, forming 2 equiv of species **2**, which is also consistent with the experiments. The spin states of the dinuclear Fe^{III}−O−O−Fe^{III} species, $[(cyclam)_2Fe_2^{III}O_2(CH_3CN)_2]^{4+}$, are complex in nature due to the involvement of two Fe^{III} units. The exchange coupling between the two Fe centers, along with the individual spin states of Fe, leads to a total of six possible spin states, for instance, ^{11}**int2**$_{(hs,hs)}$, ^{7}**int2**$_{(is,is)}$, ^{3}**int2**$_{(ls,ls)}$, ^{1}**int2**$_{(hs,hs)}$, ^{1}**int2**$_{(is,is)}$, and ^{1}**int2**$_{(ls,ls)}$ (Table 1). Among them, the ^{1}**int2**$_{(ls,ls)}$ state is the lowest in energy, and its formation is exothermic by 73.0 kJ/mol from **1** (Figure S2 and Tables S1 and S2). The two Fe^{III} centers are antiferromagnetically coupled at the ground state (S = $^1/_2$ at each Fe^{III} center) with a J value of −123 cm^{-1}. In ^{1}**int2**$_{(ls,ls)}$, the Fe−O bond length (1.828 Å) is reduced relative to ^{1}**int1** (2.170 Å) and the O1−O2 bond distance is increased to 1.454 Å (from 1.240 in ^{1}**int1**), indicating the formation of an O−O single bond attached to the Fe^{III} centers (Figure 4a). The other spin states, ^{11}**int2**$_{(hs,hs)}$, ^{7}**int2**$_{(is,is)}$, ^{3}**int2**$_{(ls,ls)}$, ^{1}**int2**$_{(hs,hs)}$, and ^{1}**int2**$_{(is,is)}$, are 82.5, 82.2, 31.1, and 68.9 kJ/mol higher in energy relative to ^{1}**int2**$_{(ls,ls)}$, respectively. Despite having a large energy separation from the lowest-lying state, the high exothermicity of all of these states from the reactant makes them capable of taking part in further reactions. The intrinsic barrier for the formation of Fe^{IV}=O species via the O−O homolytic bond cleavage in the ground state, ^{1}**ts1**$_{(ls,ls)}$ (Figures 4b and S2), is estimated to be 51.7 kJ/mol. The

https://doi.org/10.1021/acs.inorgchem.4c00371
Inorg. Chem. 2024, 63, 9809−9822

Table 1. Various Electronic Configurations Derived from DFT and Their Corresponding Relative Energies of int2 and ts1

Fe1	Fe2	species	energy (kJ/mol)
$(d_{xy})^{\uparrow}(d_{xz})^{\uparrow}(d_{yz})^{\uparrow}(d_{x^2-y^2})^{\uparrow}(d_{z^2})^{\uparrow}$	$(d_{xy})^{\uparrow}(d_{xz})^{\uparrow}(d_{yz})^{\uparrow}(d_{x^2-y^2})^{\uparrow}(d_{z^2})^{\uparrow}$	^{11}**int2**$_{(hs,hs)}$	82.5
$(d_{xy})^{\uparrow\downarrow}(d_{xz})^{\uparrow}(d_{yz})^{\uparrow}(d_{x^2-y^2})^{\uparrow}$	$(d_{xy})^{\uparrow\downarrow}(d_{xz})^{\uparrow}(d_{yz})^{\uparrow}(d_{x^2-y^2})^{\uparrow}$	^{7}**int2**$_{(is,is)}$	82.2
$(d_{xy})^{\uparrow\downarrow}(d_{xz})^{\uparrow\downarrow}(d_{yz})^{\uparrow}$	$(d_{xy})^{\uparrow\downarrow}(d_{xz})^{\uparrow\downarrow}(d_{yz})^{\uparrow}$	^{3}**int2**$_{(ls,ls)}$	31.1
$(d_{xy})^{\uparrow}(d_{xz})^{\uparrow}(d_{yz})^{\uparrow}(d_{x^2-y^2})^{\uparrow}(d_{z^2})^{\uparrow}$	$(d_{xy})^{\downarrow}(d_{xz})^{\downarrow}(d_{yz})^{\downarrow}(d_{x^2-y^2})^{\downarrow}(d_{z^2})^{\downarrow}$	^{1}**int2**$_{(hs,hs)}$	68.9
$(d_{xy})^{\uparrow\downarrow}(d_{xz})^{\uparrow}(d_{yz})^{\uparrow}(d_{x^2-y^2})^{\uparrow}$	$(d_{xy})^{\uparrow\downarrow}(d_{xz})^{\downarrow}(d_{yz})^{\downarrow}(d_{x^2-y^2})^{\downarrow}$	^{1}**int2**$_{(is,is)}$	–
$(d_{xy})^{\uparrow\downarrow}(d_{xz})^{\uparrow\downarrow}(d_{yz})^{\uparrow}$	$(d_{xy})^{\uparrow\downarrow}(d_{xz})^{\uparrow\downarrow}(d_{yz})^{\downarrow}$	^{1}**int2**$_{(ls,ls)}$	0.0
$(d_{xy})^{\uparrow}(d_{xz})^{\uparrow}(d_{yz})^{\uparrow}(d_{x^2-y^2})^{\uparrow}(d_{z^2})^{\uparrow}$	$(d_{xy})^{\uparrow}(d_{xz})^{\uparrow}(d_{yz})^{\uparrow}(d_{x^2-y^2})^{\uparrow}(d_{z^2})^{\uparrow}$	^{11}**ts1**$_{(hs,hs)}$	218.1
$(d_{xy})^{\uparrow\downarrow}(d_{xz})^{\uparrow}(d_{yz})^{\uparrow}(d_{x^2-y^2})^{\uparrow}$	$(d_{xy})^{\uparrow\downarrow}(d_{xz})^{\uparrow}(d_{yz})^{\uparrow}(d_{x^2-y^2})^{\uparrow}$	^{7}**ts1**$_{(is,is)}$	212.6
$(d_{xy})^{\uparrow\downarrow}(d_{xz})^{\uparrow\downarrow}(d_{yz})^{\uparrow}$	$(d_{xy})^{\uparrow\downarrow}(d_{xz})^{\uparrow\downarrow}(d_{yz})^{\uparrow}$	^{3}**ts1**$_{(ls,ls)}$	68.2
$(d_{xy})^{\uparrow}(d_{xz})^{\uparrow}(d_{yz})^{\uparrow}(d_{x^2-y^2})^{\uparrow}(d_{z^2})^{\uparrow}$	$(d_{xy})^{\downarrow}(d_{xz})^{\downarrow}(d_{yz})^{\downarrow}(d_{x^2-y^2})^{\downarrow}(d_{z^2})^{\downarrow}$	^{1}**ts1**$_{(hs,hs)}$	170.1
$(d_{xy})^{\uparrow\downarrow}(d_{xz})^{\uparrow}(d_{yz})^{\uparrow}(d_{x^2-y^2})^{\uparrow}$	$(d_{xy})^{\uparrow\downarrow}(d_{xz})^{\downarrow}(d_{yz})^{\downarrow}(d_{x^2-y^2})^{\downarrow}$	^{1}**ts1**$_{(is,is)}$	143.2
$(d_{xy})^{\uparrow\downarrow}(d_{xz})^{\uparrow\downarrow}(d_{yz})^{\uparrow}$	$(d_{xy})^{\uparrow\downarrow}(d_{xz})^{\uparrow\downarrow}(d_{yz})^{\downarrow}$	^{1}**ts1**$_{(ls,ls)}$	51.7

energy requirement for this step is comparatively lower (37.1 kJ/mol; see Figure 2b) on the triplet surface, which results from the ferromagnetic coupling of the two $S = {}^{1}/_{2}$ states. **ts1** leads to the formation of two molecules of **2** (product complex 1, **pc1**; Figure 2b), which are bound via van der Waals interactions. This step is strongly exothermic for the species forming from the $S = {}^{11}/_{2}$ (−160.1 kJ/mol), $S = {}^{7}/_{2}$ (−226.5 kJ/mol), and $S = 0$ (−107.2 kJ/mol) states. This dimeric species in the next step forms two molecules of Fe^{IV}═O; however, this step is slightly energy-demanding (>50 kJ/mol in the $S = {}^{3}/_{2}$ state) (Figure 2b). The formation of a dimer (**int2**) via the interaction of **int1** with a second molecule of **1** as well as the key O−O bond cleavage step is facilitated by several noncovalent interactions ranging between 2 and 2.5 Å between the N−H bonds of the ligands and the O−O moiety (Figure S3). This probably weakens the O−O bond and decreases the kinetic requirement substantially. This ability to form hydrogen-bonding interactions between the N−H groups of the cyclam ligand and O−O of the superoxo or peroxo moieties is the unique characteristic feature of the chosen ligand architecture that aids the cleveage of the O−O bond easily, allowing us to rationalize the nonrequirement of any external proton and electron sources.

In order to affirm the presence of these hydrogen-bonding interactions, QTAIM analysis was performed on the optimized geometries of ^{1}**int2** and ^{1}**ts1**. The molecular graphs generated from the QTAIM analysis are displayed in Figure S3d,e. From the QTAIM-simulated molecular graphs, it is conspicuous that BCPs exist (circled in green in Figure S3d,e) between the N−H groups in the ligand skeleton and the oxygen atoms of the Fe(III)−O−O−Fe(III) bond in both ^{1}**int2** and ^{1}**ts1**, confirming the presence of hydrogen bonds between these groups. These noncovalent interactions are responsible for the extensive stabilization of the two molecules of **2** after their formation from **int2**. This is in line with the endothermicity of the formation of **2** from the dimeric **pc1** complex. Furthermore, to verify the role of noncovalent interactions in O_2 activation and FeIV═O complex generation, we calculated the activation barrier for O−O bond cleavage without hydrogen bonds by replacing the N−H groups with N−Me groups (denoted as ^{1}**ts1**′$_{(ls,ls)}$ in Figure 4c). This resulted in a remarkably high computed barrier of 274.7 kJ/mol. In the absence of hydrogen bonding, the Fe−O bond lengths decreased from around 1.825 Å (in the presence of hydrogen bonds) to 1.776 Å. Similarly, the O−O bond was also found to be shortened from 1.846 Å (in the presence of N−H groups) to 1.745 Å (in the presence of N−Me groups), indicating that hydrogen bonds play a vital role in elongating and weakening the O−O bond in the transition state, thereby helping in diminishing the energy penality. In addition to this, the steric hindrance due to the presence of N−Me groups, shown in the space-filling model in Figure 4c, also adds to the energy penalty of ^{1}**ts1**′$_{(ls,ls)}$. Thus, the substantial activation barrier estimated upon methyl group substitution indicates that formation of the reactive Fe^{IV}═O complex is not feasible. This is in line with experimental observations where upon replacing N−H groups with N−Me groups rendered the complex unreactive toward dioxygen.

To ascertain further the obtained geometries/energetics, we computed the absorption features and Mössbauer data (see Computational Details). The TD-DFT calculations reveal a characteristic peak at 241 nm (MLCT, $\pi^{*}_{yz} \rightarrow$ L) for **1** and characteristic peaks at 352 nm (exptl λ_{max} = 330 nm; LMCT, π^{*}(O−O) $\rightarrow \delta^{*}_{z^2}$) and 455 nm (exptl λ_{max} = 455 nm; LMCT, L $\rightarrow \pi^{*}_{yz}$) for ^{1}**int1**. For species **2**, a strong feature at 567 nm was estimated due to the transition from the π^{*}_{xz} orbital to the $\delta^{*}_{x^2-y^2}$ orbital, and this is also consistent with the experiments (583 nm) (Figure S4). The isomer shift and quadrupole splitting (δ; ΔE_Q) values were computed to be 0.53; 1.144 (0.53; 0.61), 0.3; −3.730 (0.27; −2.85), and 0.07; 1.786 (0.05; 2.49) (experimental values are in parentheses) for **1**, ^{1}**int1**, and **2**, respectively.

Reactivity of Fe^{IV}═O Species toward 2,6-Di-*tert*-butylphenol. *Mechanism for the First Cycle.* To understand the unprecedented reactivity of the Fe^{IV}═O species (mentioned above) as compared to other Fe^{IV}═O species, we explored the mechanistic details (Figure 5 and Tables S4−S7) of the reaction of **2** with 2,6-di-*tert*-butylphenol (DTBP). The reaction is initiated when DTBP comes into the vicinity of **2**, forming a reactant-complex species (**rc1**: −32.7 kJ/mol on the $S = 1$ surface) where the Fe^{IV}═O complex and the substrate are held via a weak N−H(**2**)···O(DTBP) interaction (1.854 Å; Figure S5a). In the next step, the phenolic hydrogen is abstracted by **2**, forming **int3**. The first hydrogen abstraction is found to be barrierless on the quintet surface, while it possesses a small barrier of 0.2 kJ/mol on the ground $S = 1$ surface, indicating the involvement of a two-state reactivity scenario.[40,41] In ^{3}**ts2**, the Fe−O bond is elongated to 1.668 Å with the newly forming O−H and cleaving C−H (substrate) bond lengths of 1.570 and 1.012 Å, respectively, indicating an early transition state where the hydrogen has already been partially transferred to the Fe^{IV}═O center (Figure S5b).

https://doi.org/10.1021/acs.inorgchem.4c00371
Inorg. Chem. 2024, 63, 9809−9822

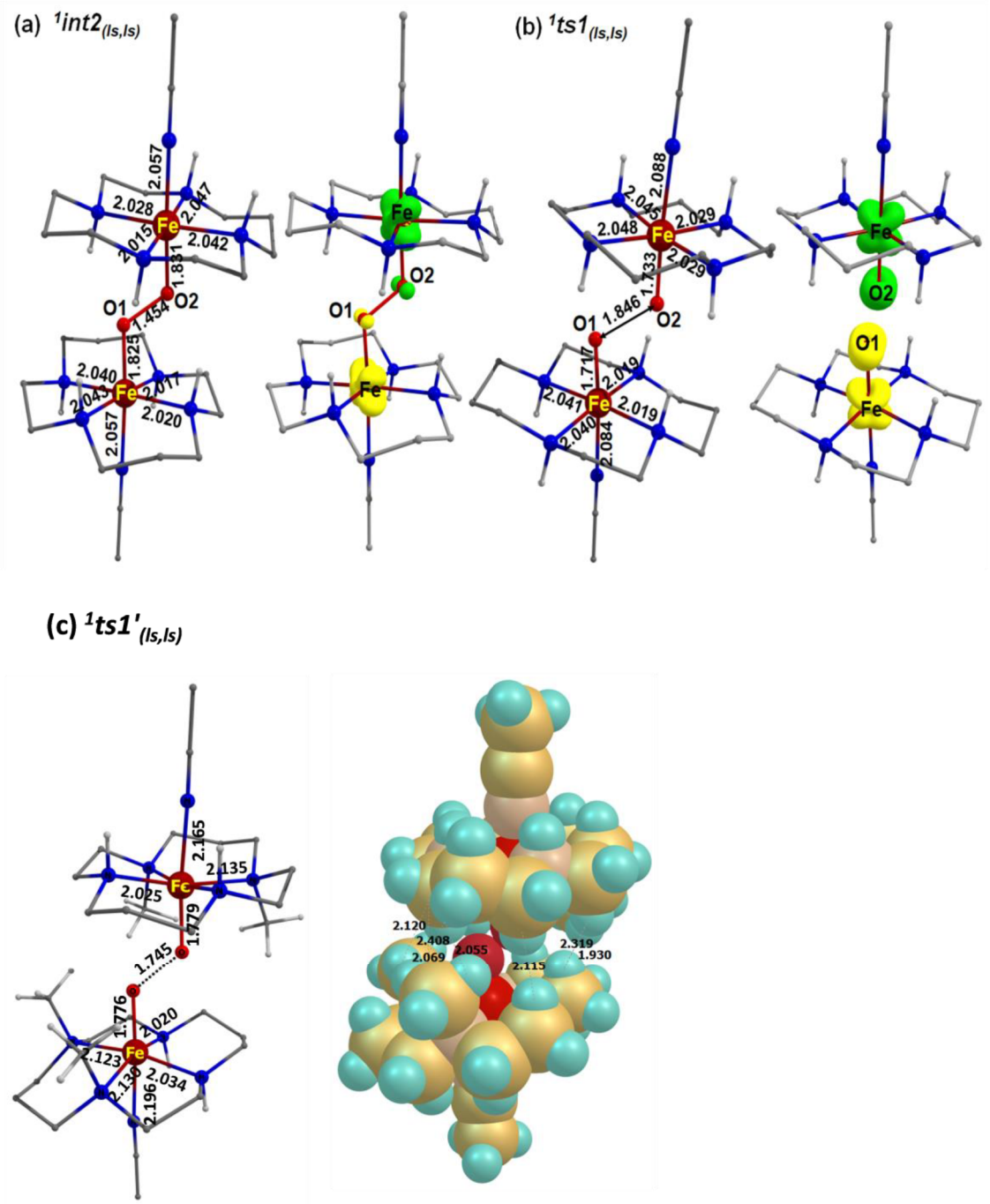

Figure 4. DFT-computed optimized structures and spin densities of (a) ^{1}**int2**$_{(ls,ls)}$, (b) ^{1}**ts1**$_{(ls,ls)}$, followed by optimized structure of (c) ^{1}**ts1′**$_{(ls,ls)}$. The Fe, O, N, C, and H atoms are shown in brown, red, blue, gray, and white color, respectively. The green and yellow isosurfaces represent the α and β spin densities, respectively.

A slight increase (0.108) in the spin densities of Fe with a decrease (0.096) on the connected oxyl center (Table S3) and no concomitant spins (a large Mulliken charge on the H atom (ρ = −0.008, e = 0.403) and O1 atom (ρ = 0.024, e = −0.606)) on the substrate indicates a proton transfer−electron transfer (PT−ET) mechanism. In **int3**, the unpaired spins on the Fe center couple ferromagnetically or antiferromagnetically with the newly generated radical on the substrate, assuming six possible spin states, namely, ^{7}**int3**$_{(hs,u)}$, ^{5}**int3**$_{(hs,d)}$, ^{5}**int3**$_{(is,u)}$, ^{3}**int3**$_{(is,d)}$, ^{3}**int3**$_{(ls,u)}$, and ^{1}**int3**$_{(ls,d)}$. Among them, ^{3}**int3**$_{(ls,u)}$ is found to be the lowest (−67.4 kJ/mol from **rc1**) in energy. At the ^{3}**int3**$_{(ls,u)}$ species, significant development in the spin density was found on the substrate (0.617), indicating the transfer of a spin-down (β) electron from the substrate to the ferryl oxygen (Figure 6a). The other spin states ^{7}**int3**$_{(hs,u)}$, ^{5}**int3**$_{(hs,d)}$, and ^{5}**int3**$_{(is,u)}$ are 19.2, 18.7, and 64.3 kJ/mol from ^{3}**int3**$_{(ls,u)}$, respectively.

The spin density on ^{3}**int3**$_{(ls,u)}$ indicates that it is not formed from a PT−ET mechanism in the triplet surface but from a barrierless quintet surface following a concerted mechanism. In the next step, a −OH rebound is expected via **ts3**, leading to the formation of a hydroxylated product (**p1**). Among several

https://doi.org/10.1021/acs.inorgchem.4c00371
Inorg. Chem. 2024, 63, 9809−9822

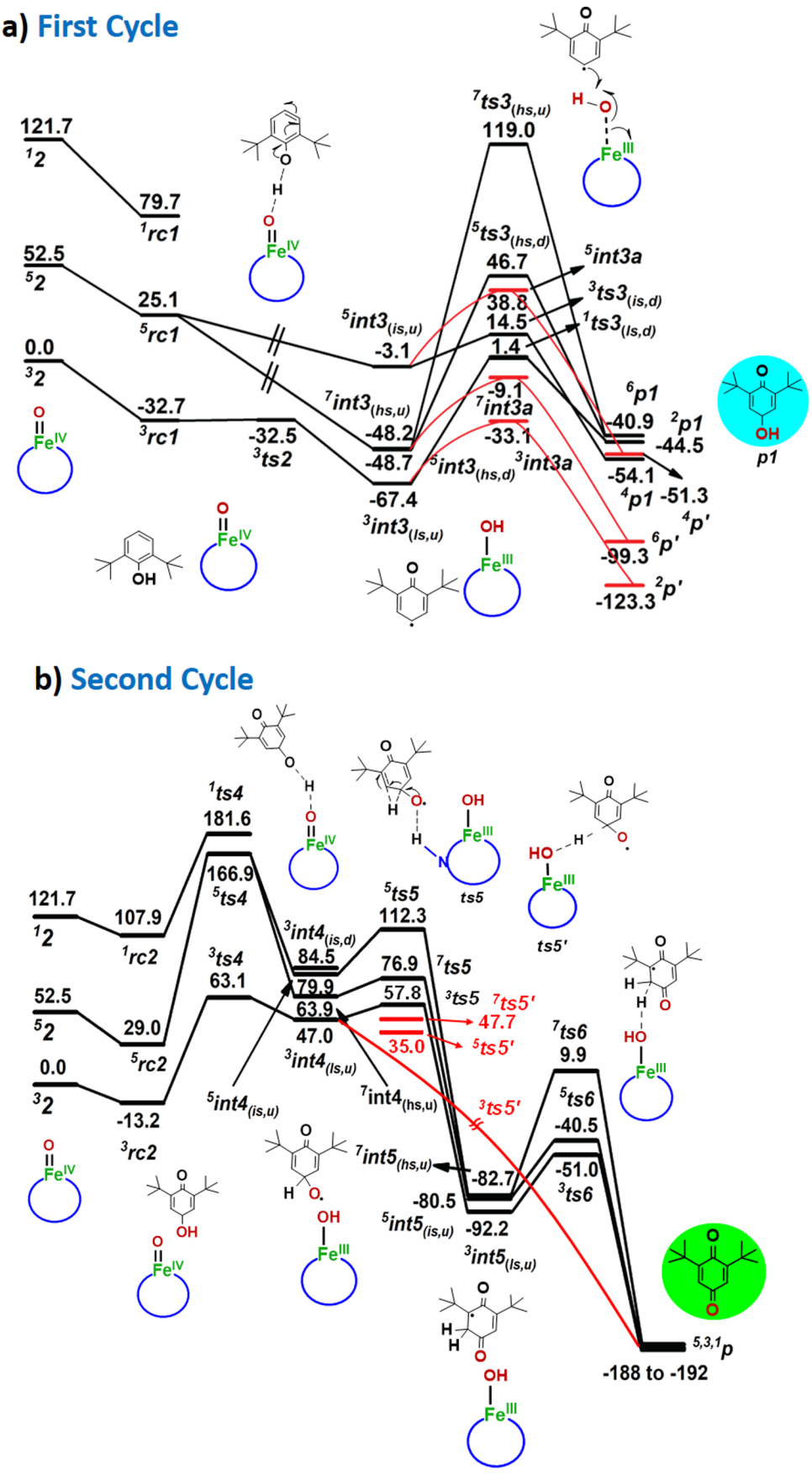

Figure 5. DFT-computed potential energy surface diagram for the first and second cycles for the formation of (a) DPT (**p′**) and (b) DTQ (**p**) from **2**. The red curve in (a) denotes the energetics of cage escape followed by C−C coupling to form **p′**, while the red curve in (b) denotes the energetics calculated for the direct hydrogen abstraction pathway.

https://doi.org/10.1021/acs.inorgchem.4c00371
Inorg. Chem. 2024, 63, 9809−9822

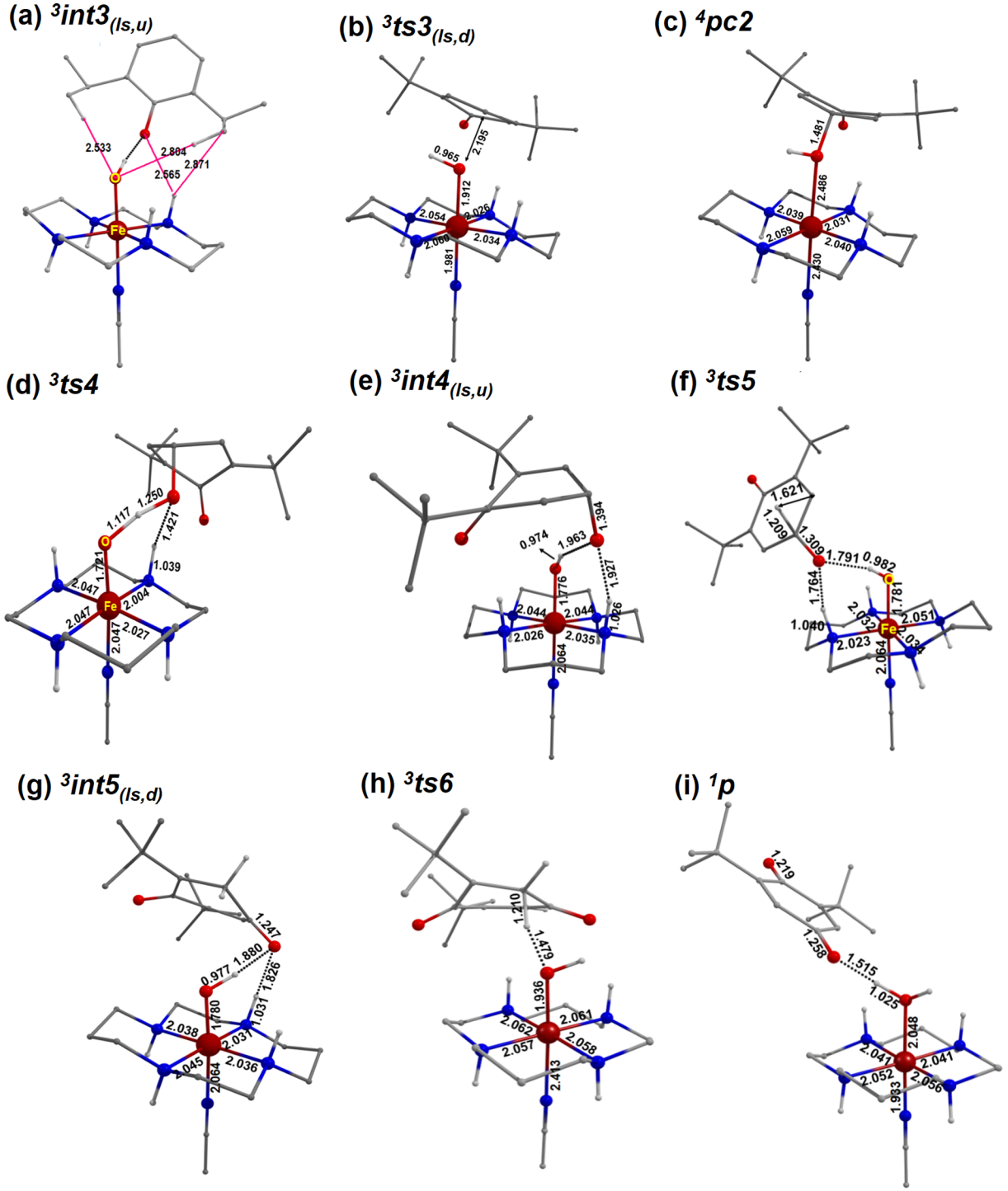

Figure 6. DFT-computed optimized structures of (a) ^{3}**int3**$_{(ls,u)}$, (b) ^{3}**ts3**$_{(ls,d)}$, (c) ^{4}**pc2**, (d) ^{3}**ts4**, (e) ^{3}**int4**$_{(ls,u)}$, (f) ^{3}**ts5**, (g) ^{3}**int5**$_{(ls,d)}$, (h) ^{3}**ts6**, and (i) ^{1}**p**. The Fe, O, N, C and H atoms are shown in brown, red, blue, gray, and white color, respectively.

spin states (Table S5) computed for **ts3**, the lowest barrier is found at the S = 0 surface (^{1}**ts3**$_{(ls,d)}$; Figure 6b), which is 68.8 kJ/mol from ^{3}**int3**$_{(ls,u)}$ resulting from the antiferromagnetic coupling between a doublet Fe^{III} state and a radical. With the ground state being ferromagnetic and featuring a barrier of 81.9 kJ/mol, this provides a sophisticated illustration of a two-state reactivity type scenario but with the involvement of exchange-coupled states that eliminates the need for forbidden spin inversion, thereby facilitating a facile reaction. As small structural modifications are known to alter the sign of J values, a significant energy penalty required for the inversion is completely circumvented.[42,43] In ^{1}**ts3**$_{(ls,d)}$, the Fe−O(H) bond length is estimated to be 1.912 Å, while the distance between the substrate and the attacking hydroxyl group is 2.195 Å. The radical character on the substrate is found to be diminished, resulting in a negligible spin density on the substrate (0.032). This results in the formation of the hydroxylated product **p1**, which is stabilized on the $S = {}^{3}/_{2}$ surface. The ^{4}**p1** state is slightly endothermic due to loss of aromaticity (by 13.3 kJ/mol) compared to **int3**, but it is exothermic by 54.1 kJ/mol

https://doi.org/10.1021/acs.inorgchem.4c00371
Inorg. Chem. 2024, 63, 9809−9822

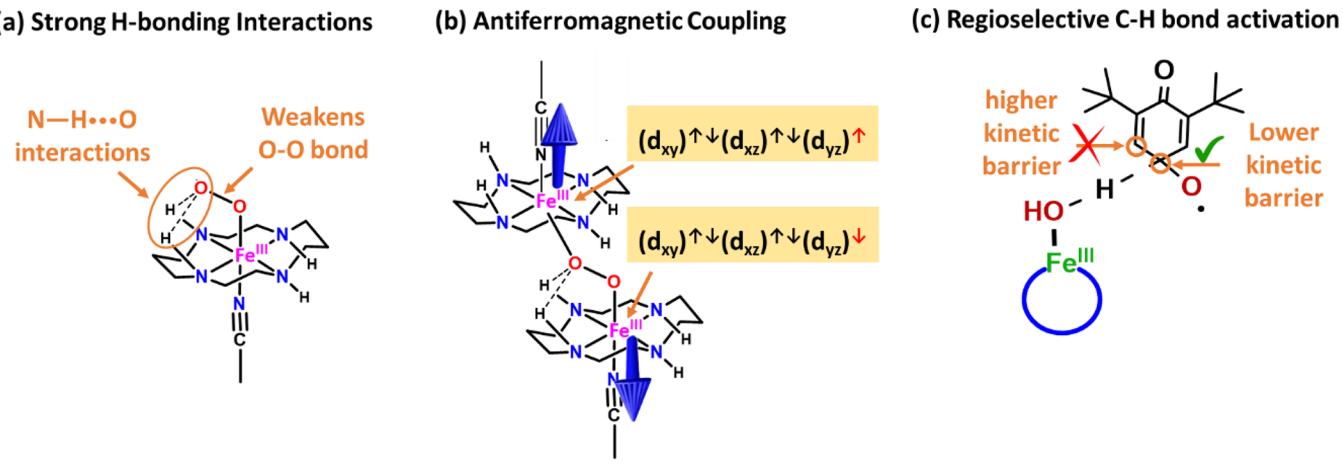

Figure 7. Three key factors that contribute to the unprecedented DTQ formation of Fe^{IV}=O and unique reactivity toward C−H bond activation.

from the reactant, suggesting facile formation of the **p1** product. In the hydroxylated product, the Fe−O(H) bond is elongated to 2.486 Å (^{4}**pc2**), with the newly formed (sub)C−O(Fe) bond length of 1.481 Å. The bonding parameters indicate that the newly formed O−H bond is still attached to the catalyst (Figure 6c), and a slight energy is required (∼20 kJ/mol) to break the Fe−O(H) bond, forming the free hydroxylated product (**p1**).

To understand the formation of multiple products that are observed in the experiments, another mechanism from **int3** is presumed, wherein the radical formed undergoes cage escape, leading to dimerization (**p'**). The energy required for the cage escape is estimated to be +34.2 kJ/mol on the triplet surface. This step is endothermic, albeit with a relatively smaller energy penalty. This small energy requirement also rationalizes the 23% yield of the dimeric product that is observed in this reaction. Between the two cases, cage-trapped and cage-escape, **int3** corresponding to the cage-trapped case is relatively more stable and has a relatively modest barrier for the rebound, resulting in the reaction diverging in both channels, rationalizing the observed major and minor products. The radical substrate formed from the activation of the O−H bond is anchored on the catalyst in **int3** via several noncovalent interactions such as C−H···O, N−H···π, etc. within the range of 2.9 Å (Figure 6a), that is facilitated only in the *trans* cyclam isomer of **2**, and therefore, the ligand design becomes a crucial factor to witness this reaction and rationalizes the unique reactivity of these Fe^{IV}=O catalysts compared to others.

Mechanism for the Second Cycle. In the next step, the mechanism of quinone formation from **p1** is assumed to occur via a second Fe^{IV}=O species as a catalyst. As isotopic labeling studies clearly illustrate the insertion of the ferryl oxygen atom from the Fe^{IV}=O unit and the requirement of 2 equiv. of Fe^{IV}=O species to produce the major product, the involvement of a second Fe^{IV}=O in the mechanism is justified. To begin with, a reactant complex (**rc2**) was assumed, which is anchored to the catalyst via several noncovalent interactions, similar to **rc1**. The formation of the second reactant complex is slightly exothermic (−13.2 kJ/mol) from the free catalyst and is most stable on the triplet surface. The hydroxylated product is found to adhere to the catalyst via two N−H···O interactions (1.903 and 1.852 Å) and one Fe−O···H(substrate) interaction (1.821 Å) (Figure S6). The lower stability of **rc2** compared to **rc1** is attributed to the higher steric crowding around the catalyst due to the hydroxyl moiety (Figure S7).

This is followed by the activation of the O−H bond by the Fe^{IV}=O routed via **ts4**, which leads to the formation of the Fe^{III}−OH intermediate (**int4**) (Figure 6e). Among different spin surfaces, the smallest O−H activation barrier is detected on the triplet surface (63.1 kJ/mol). Interestingly, the quintet surface was found to have a much higher energy penalty, suggesting the involvement of the triplet state in activating the O−H bond, unlike in the C−H bond activation by the Fe^{IV}=O species.[45] In ^{3}**ts4** (Figure 6d), the Fe−O bond is elongated to 1.721 Å, and the hydroxyl hydrogen maintains an equal distance from the catalyst and substrate oxygen (∼1.183 Å). A slight increase of spin-up (α) electron on the metal (0.098) and a decrease in the oxyl-center atom (0.184) with no significant change in the spin density on the substrate indicates a PT−ET type mechanism. The energy requirement on the quintet surface is comparatively higher, and the spin density indicates a concerted mechanism. The formation of ^{3}**int4** is exothermic by 16.4 kJ/mol. A significant spin density is found to accumulate in ^{3}**int4** (∼0.3), with a decrease in the α spin density on the metal. This indicates that although a PT−ET mechanism is favorable for the second hydrogen abstraction, subsequent electron transfer occurs before the generation of **int4**.

In the next step, 1,2 migration of the C(sp^3)−H attached species is assumed in the presence of the Fe^{III}−OH species. The oxygen atom of the OH group is anchored firmly with the Fe^{III}−OH and N−H groups (1.764 Å) of the catalyst, facilitating this migration. This migration in the presence of a catalyst via ^{3}**ts5** has a barrier of only 10.8 kJ/mol and is found to have a steeper kinetic barrier in the absence of the catalyst (>80 kJ/mol). This leads to the exothermic formation of ^{3}**int5** (−92.2 kJ/mol). The high exothermicity of ^{3}**int5** is attributed to the formation of a six-membered chelate ring, including the (catalyst)NH···(sub)O···(catalyst)Fe−O(H) moiety (Figure 6g). The involvement of these groups was again found to be responsible for easing the 1,2-migration process. In the next step, a direct hydrogen abstraction of the newly shifted hydrogen atom takes place with a barrier of 29.0 kJ/mol via ^{5}**ts6** (Figure 6h), and the final product (**p**) is exothermically stabilized by >188 kJ/mol on all surfaces (Figure 6i). It is rather unusual for the Fe^{III}−OH group to abstract the C−H bonds, and this is facilitated here with an extremely small

https://doi.org/10.1021/acs.inorgchem.4c00371
Inorg. Chem. 2024, 63, 9809−9822

barrier due to the very strong noncovalent interaction between the substrate and the catalyst. Particularly, the N−H···O, C−H···O, Fe^{III}−O(H)···O, and C−H···O(H)−Fe^{III} interactions seen in ^{3}**int5** are key to regiospecific C−H bond activation leading to the formation of DTQ. In order to verify the presence of these interactions, QTAIM analysis was performed on ^{3}**int5**, and the corresponding molecular graph generated is shown in Figure S8. From the molecular graph, it is clear that the BCPs for the aforementioned interactions do exist, confirming the presence of such strong hydrogen-bonding interaction.

Alternatively, instead of undergoing 1,2-migration, the Fe^{III}−OH species could directly abstract the hydrogen atom of the C(sp^3)−H bond via **ts5′**, leading to the formation of the product. Notably, the computed energies indicate that the specific pathway is devoid of barriers on the triplet surface (^{3}**ts5′**), whereas the quintet and septet transition states are calculated to be at 35.0 and 47.7 kJ/mol, respectively, relative to the reactant. This suggests that although 1,2-migration is also kinetically feasible, a direct hydrogen abstraction pathway is comparatively more favorable. The overall energetic gain during this process is estimated to be ∼190 kJ/mol, playing as a driving force for the forward reaction. The formation of ^{3}**ts4** is found to be the rate-determining transition state from ^{3}**rc2**, leading to a barrier of 76.3 kJ/mol.

Thus, the unprecedented DTQ formation from Fe^{IV}=O and its unique reactivity toward C−H bond activation were found to be attributed to three factors (Figure 7): (a) strong anchoring of the radical at the catalyst aided by the N−H bonds (at various intermediates; see the SI), (b) the radical anchored coupled to the Fe centers antiferromagnetically or ferromagnetically and the switch between the two states representing two-state reactivity and diminished kinetic barrier, and (c) relatively small barrier for regioselective C−H bond activation, which is critical to DTQ production, again due to noncovalent interactions and substrate positioning.

CONCLUSIONS

In summary, using DFT calculations, we explored the mechanism of the formation of a putative [(cyclam)Fe-(CH_3CN)(O)]$^{2+}$ species via a unique dimolecular activation of O_2 at a mononuclear Fe(II) center. Our calculations reproduce not only all the experimental spectroscopic data but also various spin states that are characterized. For the first time, a mechanism for the formation of Fe^{IV}=O species from the Fe^{II} precursor without the involvement of any proton/electron source routing via Fe^{III}−$O_2^{-\bullet}$ and the Fe^{III}−O_2−Fe^{III} dimer is proposed. The ligand architecture is found to play an important role in this scenario, both in the formation of a dimeric species and in the generation of putative Fe^{IV}=O species and its reactivity toward phenol oxidation. Particularly, the N−H bonds of the tetramethylcyclam ligand were found to aid the cleavage of the Fe^{III}−O−O−Fe^{III} bond homolytically by forming hydrogen bonds with the O_2 moiety, leading to a significantly lowered kinetic energy barrier. This was confirmed by performing QTAIM analysis. This feature is reasoned out to be the key factor for the observed unique reactivity of the chosen complex toward O−H and C−H activation without the requirement of any proton or electron donors. Furthermore, the roles of magnetic coupling and the spin states of the individual Fe^{III} centers are found to be important. The unprecedented formation of a quinone from alcohol by the Fe^{IV}=O complex is attributed to the nature of the ligand design, substrate positioning, and a favorable switch in the magnetic coupling that diminishes the O−H as well as C−H bond activation barriers. Given that sMMO enzymes possess numerous amino acid residues that adeptly execute such functions, it becomes imperative to integrate such secondary coordination sphere effects into the framework of prospective design strategies.

ASSOCIATED CONTENT

Supporting Information

The Supporting Information is available free of charge at https://pubs.acs.org/doi/10.1021/acs.inorgchem.4c00371.

Mössbauer spectra of ^{57}Fe-enriched **1** in frozen acetone and CH_3CN solutions, DFT-computed optimized geometries of intermediates and transition states with QTAIM-generated molecular graphs for pertinent species, UV−vis spectra of ^{2}**1**, ^{1}**int1**, and ^{3}**2**, and tables containing relative energies, spin densities, important bond parameters, and spectroscopic data for important species (PDF)

Coordinates of the optimized structures (DOCX)

AUTHOR INFORMATION

Corresponding Authors

Gopalan Rajaraman − *Department of Chemistry, IIT Bombay, Powai, Mumbai 400076, India;* orcid.org/0000-0001-6133-3026; Email: rajaraman@chem.iitb.ac.in

Kallol Ray − *Institut für Chemie, Humboldt-Universität zu Berlin, 12489 Berlin, Germany;* orcid.org/0000-0003-2074-8844; Email: kallol.ray@chemie.hu-berlin.de

Authors

Asmita Sen − *Department of Chemistry, IIT Bombay, Powai, Mumbai 400076, India*

Neethinathan Johnee Britto − *Department of Chemistry, IIT Bombay, Powai, Mumbai 400076, India*

Dustin Kass − *Institut für Chemie, Humboldt-Universität zu Berlin, 12489 Berlin, Germany;* orcid.org/0000-0003-2832-2127

Complete contact information is available at: https://pubs.acs.org/10.1021/acs.inorgchem.4c00371

Notes

The authors declare no competing financial interest.

ACKNOWLEDGMENTS

We thank SERB (SB/SJF/2019-20/12 and CRG/2022/001697) for funding. A.S. thanks IIT Bombay for a postdoctoral fellowship. K.R. is funded by the Deutsche Forschungsgemeinschaft (DFG) (1) under Germany's Excellence Strategy—EXC 2008-390540038—UniSysCat and (2) via a Heisenberg-Professorship.

REFERENCES

(1) Ray, K.; Pfaff, F. F.; Wang, B.; Nam, W. Status of reactive non-heme metal−oxygen intermediates in chemical and enzymatic reactions. *J. Am. Chem. Soc.* **2014**, *136* (40), 13942−13958.

(2) Puri, M.; Que, L., Jr Toward the synthesis of more reactive *S* = 2 non-heme oxoiron(IV) complexes. *Acc. Chem. Res.* **2015**, *48* (8), 2443−2452.

(3) Hong, S.; Lee, Y.-M.; Ray, K.; Nam, W. Dioxygen activation chemistry by synthetic mononuclear nonheme iron, copper and chromium complexes. *Coord. Chem. Rev.* **2017**, *334*, 25−42.

(4) Krebs, C.; Galonic Fujimori, D.; Walsh, C. T.; Bollinger, J. M., Jr. Non-heme Fe(IV)−oxo intermediates. *Acc. Chem. Res.* **2007**, *40* (7), 484−492.
(5) Solomon, E. I.; Goudarzi, S.; Sutherlin, K. D. O_2 activation by non-heme iron enzymes. *Biochemistry* **2016**, *55* (46), 6363−6374.
(6) Bryliakov, K. P.; Talsi, E. P. Active sites and mechanisms of bioinspired oxidation with H_2O_2, catalysed by non-heme Fe and related Mn complexes. *Coord. Chem. Rev.* **2014**, *276*, 73−96.
(7) Jasniewski, A. J.; Que, L., Jr Dioxygen activation by nonheme diiron enzymes: Diverse dioxygen adducts, high-valent intermediates, and related model complexes. *Chem. Rev.* **2018**, *118* (5), 2554−2592.
(8) Castillo, R. G.; Banerjee, R.; Allpress, C. J.; Rohde, G. T.; Bill, E.; Que, L., Jr; Lipscomb, J. D.; DeBeer, S. High-energy-resolution fluorescence-detected X-ray absorption of the Q intermediate of soluble methane monooxygenase. *J. Am. Chem. Soc.* **2017**, *139* (49), 18024−18033.
(9) Cutsail III, G. E.; Banerjee, R.; Zhou, A.; Que, L., Jr; Lipscomb, J. D.; DeBeer, S. High-resolution extended X-ray absorption fine structure analysis provides evidence for a longer Fe···Fe distance in the Q intermediate of methane monooxygenase. *J. Am. Chem. Soc.* **2018**, *140* (48), 16807−16820.
(10) Thibon, A.; England, J.; Martinho, M.; Young, V. G., Jr; Frisch, J. R.; Guillot, R.; Girerd, J. J.; Münck, E.; Que, L., Jr; Banse, F. Proton- and Reductant-Assisted Dioxygen Activation by a Nonheme Iron(II) Complex to Form an Oxoiron(IV) Intermediate. *Angew. Chem.* **2008**, *120* (37), 7172−7175.
(11) Nishida, Y.; Lee, Y.-M.; Nam, W.; Fukuzumi, S. Autocatalytic Formation of an Iron(IV)−Oxo Complex via Scandium Ion-Promoted Radical Chain Autoxidation of an Iron(II) Complex with Dioxygen and Tetraphenylborate. *J. Am. Chem. Soc.* **2014**, *136* (22), 8042−8049.
(12) Lee, Y.-M.; Bang, S.; Kim, Y. M.; Cho, J.; Hong, S.; Nomura, T.; Ogura, T.; Troeppner, O.; Ivanović-Burmazović, I.; Sarangi, R.; Fukuzumi, S.; Nam, W. A mononuclear nonheme iron(III)-peroxo complex binding redox-inactive metal ions. *Chem. Sci.* **2013**, *4* (10), 3917−3923.
(13) Kass, D.; Corona, T.; Warm, K.; Braun-Cula, B.; Kuhlmann, U.; Bill, E.; Mebs, S.; Swart, M.; Dau, H.; Haumann, M.; Hildebrandt, P.; Ray, K. Stoichiometric formation of an oxoiron(IV) complex by a soluble methane monooxygenase type activation of O_2 at an iron(II)−cyclam center. *J. Am. Chem. Soc.* **2020**, *142* (13), 5924−5928.
(14) Tinberg, C. E.; Lippard, S. J. Dioxygen activation in soluble methane monooxygenase. *Acc. Chem. Res.* **2011**, *44* (4), 280−288.
(15) Frisch, M. J.; Trucks, G. W.; Schlegel, H. B.; Scuseria, G. E.; Robb, M. A.; Cheeseman, J. R.; Scalmani, G.; Barone, V.; Petersson, G. A.; Nakatsuji, H.; et al. *Gaussian 16*; Gaussian, Inc.: Wallingford, CT, 2016.
(16) Becke, A. D. Density-functional thermochemistry. V. Systematic optimization of exchange-correlation functionals. *J. Chem. Phys.* **1997**, *107* (20), 8554−8560.
(17) Becke, A. D. Density-functional exchange-energy approximation with correct asymptotic behavior. *Phys. Rev. A* **1988**, *38* (6), 3098.
(18) Hay, P. J.; Wadt, W. R. Ab initio effective core potentials for molecular calculations. Potentials for K to Au including the outermost core orbitals. *J. Chem. Phys.* **1985**, *82* (1), 299−310.
(19) Sen, A.; Ansari, A.; Swain, A.; Pandey, B.; Rajaraman, G. Probing the Origins of Puzzling Reactivity in Fe/Mn-Oxo/Hydroxo Species toward C-H Bonds: A DFT and Ab Initio Perspective. *Inorganic Chemistry* **2023**, *62* (37), 14931−14941.
(20) Britto, N. J.; Sen, A.; Rajaraman, G. Unravelling the Effect of Acid-Driven Electron Transfer in High-Valent Fe^{IV}= O/Mn^{IV}= O Species and Its Implications for Reactivity. *Chem. - Asian J.* **2023**, *18* (23), e202300773.
(21) Cantú Reinhard, F. n. G.; Faponle, A. S.; de Visser, S. P. Substrate sulfoxidation by an iron(IV)−oxo complex: Benchmarking computationally calculated barrier heights to experiment. *J. Phys. Chem. A* **2016**, *120* (49), 9805−9814.
(22) Ansari, A.; Kaushik, A.; Rajaraman, G. Mechanistic Insights on the ortho-Hydroxylation of Aromatic Compounds by Non-Heme Iron Complex: A Computational Case Study on the Comparative Oxidative Ability of Ferric-Hydroperoxo and High-Valent Fe^{IV}=O and Fe^{V}=O Intermediates. *J. Am. Chem. Soc.* **2013**, *135* (11), 4235−4249.
(23) Rana, S.; Biswas, J. P.; Sen, A.; Clémancey, M.; Blondin, G.; Latour, J.-M.; Rajaraman, G.; Maiti, D. Selective C-H halogenation over hydroxylation by noN-Heme iron(IV)-oxo. *Chem. Sci.* **2018**, *9* (40), 7843−7858.
(24) Kumar, R.; Pandey, B.; Sen, A.; Ansari, M.; Sharma, S.; Rajaraman, G. Role of oxidation state, ferryl-oxygen, and ligand architecture on the reactivity of popular high-valent Fe^{IV}=O species: A theoretical perspective. *Coord. Chem. Rev.* **2020**, *419*, 213397.
(25) Vyas, N.; Sen, A.; Kumar, A.; Grover, A. Computational study of ammonia generation by iron(III) and iron(IV) complexes supported by trigonal bipyramidal iron. *Int. J. Quantum Chem.* **2021**, *121* (21), No. e26775.
(26) Lundberg, M.; Siegbahn, P. E. M. Agreement between experiment and hybrid DFT calculations for O-H bond dissociation enthalpies in manganese complexes. *J. Comput. Chem.* **2005**, *26* (7), 661−667.
(27) Jayapal, P.; Ansari, A.; Rajaraman, G. Computational examination on the active site structure of a (peroxo)diiron(III) intermediate in the amine oxygenase AurF. *Inorg. Chem.* **2015**, *54*, 11077−11082.
(28) Ansari, A.; Ansari, M.; Singha, A.; Rajaraman, G. Interplay of Electronic Cooperativity and Exchange Coupling in Regulating the Reactivity of Diiron (IV)-oxo Complexes towards C- H and O- H Bond Activation. *Chem. - Eur. J.* **2017**, *23*, 10110−10125.
(29) Quesne, M. G.; Senthilnathan, D.; Singh, D.; Kumar, D.; Maldivi, P.; Sorokin, A. B.; de Visser, S. P. Origin of the Enhanced Reactivity of μ-Nitrido-Bridged Diiron(IV)−Oxo Porphyrinoid Complexes over Cytochrome P450 Compound I. *ACS Catal.* **2016**, *6*, 2230−2243.
(30) Wang, C.; Chen, H. Convergent theoretical prediction of reactive oxidant structures in diiron arylamine oxygenases AurF and CmlI: peroxo or hydroperoxo? *J. Am. Chem. Soc.* **2017**, *139*, 13038−13046.
(31) Xue, G.; Geng, C.; Ye, S.; Fiedler, A. T.; Neese, F.; Que, L., Jr. Hydrogen-Bonding Effects on the Reactivity of [X−Fe^{III}−O−Fe^{IV}−O] (X = OH, F) Complexes toward C−H Bond Cleavage. *Inorg. Chem.* **2013**, *52*, 3976−3984.
(32) Ferreira, D. E.; De Almeida, W. B.; Neves, A.; Rocha, W. R. Theoretical investigation of the reaction mechanism for the phosphate diester hydrolysis using an asymmetric dinuclear metal complex as a biomimetic model of the purple acid phosphatase enzyme. *Phys. Chem. Chem. Phys.* **2008**, *10*, 7039−7046.
(33) Grimme, S.; Antony, J.; Ehrlich, S.; Krieg, H. A consistent and accurate ab initio parametrization of density functional dispersion correction (DFT-D) for the 94 elements H-Pu. *J. Chem. Phys.* **2010**, *132*, 154104.
(34) Weigend, F. Accurate Coulomb-fitting basis sets for H to Rn. *Phys. Chem. Chem. Phys.* **2006**, *8* (9), 1057−1065.
(35) Weigend, F.; Ahlrichs, R. Balanced basis sets of split valence, triple zeta valence and quadruple zeta valence quality for H to Rn: Design and assessment of accuracy. *Phys. Chem. Chem. Phys.* **2005**, *7* (18), 3297−3305.
(36) Marenich, A. V.; Cramer, C. J.; Truhlar, D. G. Universal solvation model based on solute electron density and on a continuum model of the solvent defined by the bulk dielectric constant and atomic surface tensions. *J. Phys. Chem. B* **2009**, *113* (18), 6378−6396.
(37) Noodleman, L. Valence bond description of antiferromagnetic coupling in transition metal dimers. *J. Chem. Phys.* **1981**, *74* (10), 5737−5743.
(38) Noodleman, L.; Davidson, E. R. Ligand spin polarisation and antiferromagnetic coupling in transition metal dimers. *Chem. Phys.* **1986**, *109* (1), 131−143.

https://doi.org/10.1021/acs.inorgchem.4c00371
Inorg. Chem. 2024, 63, 9809−9822

(39) Neese, F. Software update: The ORCA program system—Version 5.0. *Wiley Interdiscip. Rev.: Comput. Mol. Sci.* **2022**, *12* (5), No. e1606.
(40) Kumar, P.; Sen, A.; Rajaraman, G.; Shanmugam, M. An unusual mixed-valence cobalt dimer as a catalyst for the anti-Markovnikov hydrophosphination of alkynes. *Inorg. Chem. Front.* **2022**, *9* (10), 2161−2172.
(41) Sen, A.; Vyas, N.; Pandey, B.; Rajaraman, G. Deciphering the mechanism of oxygen atom transfer by Non-Heme Mn^{IV}-oxo species: an ab initio and DFT exploration. *Dalton Trans.* **2020**, *49* (30), 10380−10393.
(42) Garcia-Ratés, M.; Neese, F. Efficient implementation of the analytical second derivatives of Hartree-Fock and hybrid DFT energies within the framework of the conductor-like polarizable continuum model. *J. Comput. Chem.* **2019**, *40*, 1816−1828.
(43) Römelt, M.; Ye, S.; Neese, F. Calibration of modern density functional theory methods for the prediction of ^{57}Fe Mössbauer isomer shifts: meta-GGA and double-hybrid functionals. *Inorg. Chem.* **2009**, *48* (3), 784−785.
(44) Biegler-König, F.; Schönbohm, J. Update of the AIM2000-Program for Atoms in Molecules. *J. Comput. Chem.* **2002**, *23* (15), 1489−1494.
(45) Hunter, T.; McNae, I.; Liang, X.; Bella, J.; Parsons, S.; Walkinshaw, M.; Sadler, P. Protein recognition of macrocycles: Binding of anti-HIV metallocyclams to lysozyme. *Proc. Natl. Acad. Sci. U.S.A.* **2005**, *102*, 2288−92.
(46) Chen, H.; Ikeda-Saito, M.; Shaik, S. Nature of the Fe−O_2 Bonding in Oxy-Myoglobin: Effect of the Protein. *J. Am. Chem. Soc.* **2008**, *130*, 14778−14790.
(47) Schröder, D.; Shaik, S.; Schwarz, H. Two-State Reactivity as a New Concept in Organometallic Chemistry. *Acc. Chem. Res.* **2000**, *33* (3), 139−145.
(48) Shaik, S. Two-State Reactivity: Personal Recounting of its Conception and Future Prospects. *Isr. J. Chem.* **2020**, *60* (10−11), 938−956.
(49) Mondal, D.; Majee, M. C.; Bhattacharya, K.; Long, J.; Larionova, J.; Khusniyarov, M. M.; Chaudhury, M. Crossover from Antiferromagnetic to Ferromagnetic Exchange Coupling in a New Family of Bis-(μ-phenoxido)dicopper(II) Complexes: A Comprehensive Magneto-Structural Correlation by Experimental and Theoretical Study. *ACS Omega* **2019**, *4* (6), 10558−10570.
(50) Bencini, A.; Totti, F.; Daul, C. A.; Doclo, K.; Fantucci, P.; Barone, V. Density functional calculations of magnetic exchange interactions in polynuclear transition metal complexes. *Inorg. Chem.* **1997**, *36* (22), 5022−5030.
(51) Ansari, A.; Ansari, M.; Singha, A.; Rajaraman, G. Interplay of Electronic Cooperativity and Exchange Coupling in Regulating the Reactivity of Diiron(IV)-oxo Complexes towards C-H and O-H Bond Activation. *Chem. - Eur. J.* **2017**, *23* (42), 10110−10125.

https://doi.org/10.1021/acs.inorgchem.4c00371
Inorg. Chem. 2024, 63, 9809−9822